

Exploring Beyond Λ CDM with the Weak Lensing Power Spectrum and Bispectrum

Liantsoa F. Randrianjanahary^{1,2} Chandrachud B. V. Dash¹

¹Astrophysics Research Centre & School of Mathematics, Statistics and Computer Science, University of KwaZulu-Natal, Durban, 4041, South Africa

²Department of Physics & Astronomy, University of the Western Cape, Cape Town 7535, South Africa

E-mail: fna.liantsoarandrianjanahary@gmail.com

Abstract. In this article, we investigate the effect of systematics on weak lensing beyond the standard Λ CDM paradigm. Specifically, we consider the 2- and 3-point statistics of the shear field for the set of cosmological models, including CPL dark energy, interacting dark energy (IDE), and Hu-Sawicki $f(R)$ modified gravity. We consider two major systematics such as photometric redshift uncertainty and intrinsic alignment \mathcal{A}_{IA} . Our findings are derived from the Fisher matrix. These results indicate that σ_z and \mathcal{A}_{IA} can substantially degrade constraining power, especially for $f(R)$ gravity. Moreover, it also highlights the critical role of higher-order statistics and the need for robust systematic control for future cosmological surveys.

Contents

1	Introduction	1
2	Dark energy models: background expansion and growth	3
2.1	Unified description of the background expansion	3
3	Linear growth in beyond-ΛCDM models	5
4	Weak lensing observables and systematics	9
4.1	Two-point power spectra	9
4.2	Tomographic weak lensing power spectrum	9
4.3	Intrinsic alignments (IA)	11
4.4	Photometric redshift uncertainties	11
5	Weak lensing bispectrum	12
5.1	Matter bispectrum modeling	12
5.2	Tomographic shear bispectrum	13
6	Fisher matrix formalism	15
6.1	Power spectrum Fisher matrix	15
6.2	Bispectrum Fisher matrix	15
7	Analysis and discussion	16
7.1	deviation from Λ CDM	16
7.2	Information content	18
8	Conclusion	20
9	Data Availability Statement	21
10	Code Availability Statement	21
11	Funding	21

1 Introduction

Investigating the physical cause of the late-time accelerated expansion of the universe is one of the key challenges in contemporary cosmology [1–4]. Several observations, including the cosmic microwave background, baryonic acoustic oscillations, redshift distortions, type Ia supernovae, and cosmic chronometers, support the flat Λ CDM framework, which is dominated by accelerated expansion driven by dark energy [5–8]. Within the concordance Λ CDM model, this paradigm is related to the cosmological constant Λ . Although Λ CDM provides an excellent phenomenological description of current data, it suffers from well-known theoretical issues, including the fine-tuning and coincidence problems, thereby motivating a broad class of alternatives involving dynamical dark energy or modifications of gravity on cosmological scales, such as scalar-tensor theories or modified gravity models like $f(R)$ gravity [4, 9–12].

Making such distinctions between these scenarios requires the presence of observables that are equally sensitive to the evolution of the background expansion history as well as structure. In this context, weak gravitational lensing has been considered one of the most powerful and robust cosmological probes. The foreground mass causes light rays to deflect due to changes in gravitational potential from the density field. This deflection leads to the magnification and shear of background objects. Gravitational lensing is a direct probe of the total matter distribution through coherent distortions of the shapes of background galaxies. This bypasses the need to deal with issues related to galaxy bias. Thus, weak lensing provides a good probe of the projected matter density. Tomographic weak lensing surveys such as the Dark Energy Survey (DES) [13], as well as upcoming Stage IV weak lensing surveys such as the Vera C. Rubin Observatory Legacy Survey of Space and Time (LSST) [14, 15], will provide percent-level constraints on both the Hubble expansion rate $H(a)$ and the growth factor $D(a; k)$ through the projection of the nonlinear matter power spectrum [9, 14–16].

Most analyses of weak gravitational lensing involve the study of two-point statistics, including the shear or convergence power spectrum. This signal is highly informative but only describes the Gaussian contribution to the matter density field. Hence, nonlinear gravitational evolution leads to the appearance of non-Gaussian features in the matter density field, as described by the contribution of higher correlation functions. In particular, the weak lensing bispectrum is the harmonic transform of the three-point correlation function and is responsible for mode coupling and nonlinear structure formation. A joint analysis of the power spectrum and the bispectrum has the potential to improve constraints on cosmological parameters significantly. This is because it can help to break the degeneracy partially between parameters and can also account for scale-dependent effects that are relevant to the cosmological models under consideration, including the effects of dark energy and modified gravity on the growth of structure. In this paper, we propose a general weak lensing analysis that includes a simultaneous analysis of shear power spectra and shear bispectra. We test a range of cosmological models, including those relevant to dark energy and modified gravity theories. Specifically, we consider the following extensions to the standard Λ CDM model: (i) w CDM with dynamical dark energy; (ii) an interacting dark energy model in which energy and momentum transfer are allowed within the dark sector; and (iii) the Hu-Sawicki $f(R)$ model, in which the Poisson equation is modified and a scale- and time-dependent modification of gravity occurs.

Among a wide range of systematics that can affect the weak lensing signal, two of them are critical that draw our attention in this study, including photometric redshift uncertainty and intrinsic alignment of galaxies. Unlike spectroscopic redshift, which is highly accurate, photometry uses broadband colors. Because different galaxy types at different redshifts can produce similar colors, the estimation is inherently uncertain. Photometric redshift uncertainty is the margin of error in estimating a galaxy’s distance by analyzing its light through broad-band filters rather than precise spectroscopy. It represents the difference between the estimated and true redshifts. This redshift uncertainty can degrade the cosmological information [17–20]. Galaxies are not randomly oriented but tend to align with the large-scale structure in which they reside. This creates a non-lensing correlation that can bias cosmic shear measurements. Intrinsic alignments can significantly suppress the cosmic shear power spectrum, as demonstrated by [21], and were detected for the first time in the KiDS-450 photometric survey by [22, 23]. For weak lensing, one of the main difficulties in making cosmological forecasts was the ability to accurately model the intrinsic alignments of galaxies—a local orientation of galaxies that acts to mimic the cosmological lensing signal [24]. Several

physical models have been proposed [25–30] that model intrinsic alignments in a more realistic manner, drawing increased attention in this area.

Our main objective is to quantify the cosmological information gained by combining two- and three-point weak lensing statistics. Specifically, we investigate how the inclusion of bispectrum measurements improves constraints on dynamical equation-of-state parameters, dark sector interaction strengths, and $f(R)$ gravity amplitude relative to power spectrum-only analyses. This joint approach is especially timely for next-generation surveys, where the statistical precision demands optimal extraction of all available information to robustly test the nature of dark energy and gravity. The paper is organized as follows. Sections 2 introduce the dark energy models beyond Λ CDM: background expansion and growth. Section 3 shows linear growth of structure in beyond- Λ CDM models, while sections 4 and 5 elaborate, respectively, on weak lensing observables and observational systematics and weak lensing bispectrum formalism. Section 7 is dedicated to the analysis and discussion.

2 Dark energy models beyond Λ CDM: background expansion and growth

We first present the dark energy and modified gravity scenarios under study within a unified framework for background expansion and linear structure growth before discussing the weak lensing observables.

2.1 Unified description of the background expansion

We start by writing the homogeneous expansion histories for the three dark energy/modified gravity models under investigation in a unified form, before going on to discuss the growth of perturbations. We can write the background Hubble expansion rate in the form,

$$E(a) \equiv \frac{H(a)}{H_0} = [\Omega_{m0} a^{-3} + (1 - \Omega_{m0}) \mathcal{F}_X(a)]^{1/2}, \quad (2.1)$$

where $X \in \{\Lambda\text{CDM}, w\text{CDM}, \text{IDE}, f(R)\}$ labels the model, and $\mathcal{F}_X(a)$ encodes the effective dark energy or modified gravity contribution to the expansion. In the following we specify $\mathcal{F}_X(a)$ for each case.

Λ CDM

In the concordance model, dark energy is a cosmological constant with equation of state $w = -1$ [31]. The expansion history is then

$$\mathcal{F}_{\Lambda\text{CDM}}(a) = 1, \quad E_{\Lambda\text{CDM}}^2(a) = \Omega_{m0} a^{-3} + (1 - \Omega_{m0}). \quad (2.2)$$

Dynamical dark energy ($w\text{CDM}$ / CPL)

For a dynamical dark energy component with a time-varying equation of state $w(a)$, the dark energy density scales as [32]

$$\rho_{\text{DE}}(a) = \rho_{\text{DE},0} \exp \left[-3 \int_1^a \frac{da'}{a'} (1 + w(a')) \right]. \quad (2.3)$$

In the commonly used Chevallier–Polarski–Linder (CPL) parametrization

$$w(a) = w_0 + w_a(1 - a), \quad (2.4)$$

this yields

$$\mathcal{F}_{w\text{CDM}}(a) = a^{-3(1+w_0+w_a)} \exp[-3w_a(1-a)], \quad (2.5)$$

and hence

$$E_{w\text{CDM}}^2(a) = \Omega_{m0} a^{-3} + (1 - \Omega_{m0}) a^{-3(1+w_0+w_a)} \exp[-3w_a(1-a)] \quad (2.6)$$

The ΛCDM limit is recovered for $(w_0, w_a) = (-1, 0)$.

Interacting dark energy (IDE)

In interacting dark energy models, the dark sector is coupled via an energy–momentum transfer Q between dark matter and dark energy. At the background level, the continuity equations read [33, 34]

$$\dot{\rho}_m + 3H\rho_m = +Q, \quad (2.7)$$

$$\dot{\rho}_{\text{DE}} + 3H(1+w_{\text{DE}})\rho_{\text{DE}} = -Q, \quad (2.8)$$

so that the total dark sector energy density $\rho_m + \rho_{\text{DE}}$ is conserved. We follow the notation of IDE parameters given in [33]. In the class of IDE models considered here, the interaction is parametrized as

$$Q(a) = \Gamma(a) \rho_m(a), \quad (2.9)$$

with

$$\Gamma(a) = -\alpha \sigma H(a)^{-(2\alpha+1)}, \quad \sigma = 3(1 - \Omega_{m0}) H_0^{2(\alpha+1)}, \quad (2.10)$$

so that the effective “vacuum” component obeys

$$\Lambda(a) = \sigma H(a)^{-2\alpha}. \quad (2.11)$$

The background expansion can be written compactly as

$$E_{\text{IDE}}^2(a) = \Omega_{m0} a^{-3} + (1 - \Omega_{m0}) \mathcal{F}_{\text{IDE}}(a), \quad (2.12)$$

where $\mathcal{F}_{\text{IDE}}(a)$ is determined implicitly by the coupled system above and reduces to unity in the limit $Q \rightarrow 0$ ($\Gamma \rightarrow 0$), i.e.

$$\mathcal{F}_{\text{IDE}}(a) \xrightarrow{Q \rightarrow 0} \mathcal{F}_{\Lambda\text{CDM}}(a) = 1 \quad (2.13)$$

so that $E_{\text{IDE}}(a) \rightarrow E_{\Lambda\text{CDM}}(a)$ in the non-interacting limit.

Hu–Sawicki $f(R)$ gravity

In Hu–Sawicki $f(R)$ gravity, which is studied extensively in many literature like [35–41], the Einstein–Hilbert action is modified by a function of the Ricci scalar R ,

$$S = \frac{1}{16\pi G} \int d^4x \sqrt{-g} [R + f(R)] + S_m, \quad (2.14)$$

with the specific form

$$f(R) = -m^2 \frac{c_1 (R/m^2)^n}{c_2 (R/m^2)^n + 1}, \quad (2.15)$$

where $m^2 \sim H_0^2$ and (c_1, c_2, n) are model parameters often recast in terms of f_{R0} . In the small- $(|f_R|)$ and high-curvature limit, we can write

$$f_R(a) \simeq f_{R0} \left[\frac{\Omega_{m0} a^{-3} + 4(1 - \Omega_{m0})}{\Omega_{m0} + 4(1 - \Omega_{m0})} \right]^{-2}, \quad (2.16)$$

For suitable choices of parameters, the background expansion is constructed to closely mimic a Λ CDM history,

$$E_{f(R)}^2(a) \simeq \Omega_{m0} a^{-3} + (1 - \Omega_{m0}), \quad (2.17)$$

i.e.

$$\mathcal{F}_{f(R)}(a) \simeq 1, \quad (2.18)$$

and the main impact of the modified gravity appears in the scale- and time-dependent growth of perturbations rather than in the background Hubble rate. In the limit $f_{R0} \rightarrow 0$, the model reduces exactly to GR/ Λ CDM, and Eq. (2.17) becomes identical to Eq. (2.2).

Equations (2.1)–(2.17) thus provide a compact, unified description of the background expansion across the beyond- Λ CDM scenarios that we confront with weak lensing observables.

3 Linear growth of structure in beyond- Λ CDM models

In analogy with the background expansion, we adopt a unified description of the linear growth of matter perturbations, highlighting the distinct physical mechanisms at play in each model class.

The growth of cosmological perturbations, characterized by the linear growth factor $D(z)$, and the growth rate $f(z)$, serves as a vital probe of both the Universe’s expansion history and gravitational theory. Observational efforts, such as peculiar velocity surveys and redshift-space distortion measurements, have been used to constrain the growth rate across redshift [42], while theoretical studies explore growth evolution under quintessence, $f(R)$ gravity, and scalar-tensor models [43–45]. These efforts highlight the critical role of growth observables in distinguishing between dark energy models and modified gravity. It is convenient to write the linear growth of matter perturbations in a form that explicitly separates the Hubble “drag” term from the gravitational “source” term. For all the models considered in this work, we can write

$$\frac{d^2 D(a)}{da^2} + \mathcal{D}_X(a, k) \frac{dD(a)}{da} = \mathcal{S}_X(a, k) D(a), \quad (3.1)$$

where $D(a) \equiv \delta_m(a)$ is the linear growth factor and $X \in \{\Lambda\text{CDM}, w\text{CDM}, \text{IDE}, f(R)\}$ labels the underlying cosmological model. The function $\mathcal{D}_X(a, k)$ plays the role of an effective drag (or friction) coefficient in growth, while $\mathcal{S}_X(a, k)$ encodes the net gravitational source driving the amplification of density perturbations.

This form is equivalent to the more familiar

$$\frac{d^2 D(a)}{da^2} + A_X(a, k) \frac{dD(a)}{da} + B_X(a, k) D(a) = 0, \quad (3.2)$$

upon identifying

$$\mathcal{D}_X(a, k) = A_X(a, k), \quad \mathcal{S}_X(a, k) = -B_X(a, k). \quad (3.3)$$

In what follows we give \mathcal{D}_X and \mathcal{S}_X explicitly for Λ CDM, interacting dark energy (IDE), and Hu–Sawicki $f(R)$, using $E(a) \equiv H(a)/H_0$ and Ω_{m0} .

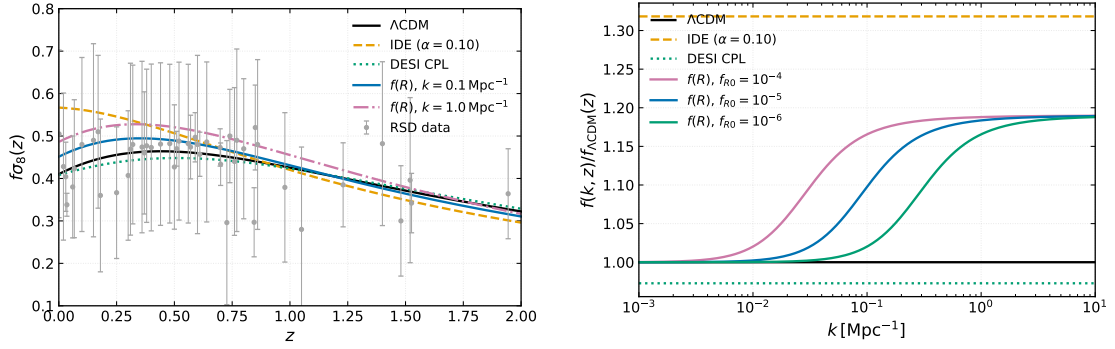


Figure 1: Left: redshift evolution of the scale-independent growth factor $f\sigma_8(z)$ for the three models considered. Data points are taken from [46]. Right: scale- and redshift-dependent growth $f\sigma_8(z; k)$ in Hu-Sawicki $f(R)$ with $\ln(f_{R0}) = -5$ at $z = 0.1$ for representative wavenumbers k .

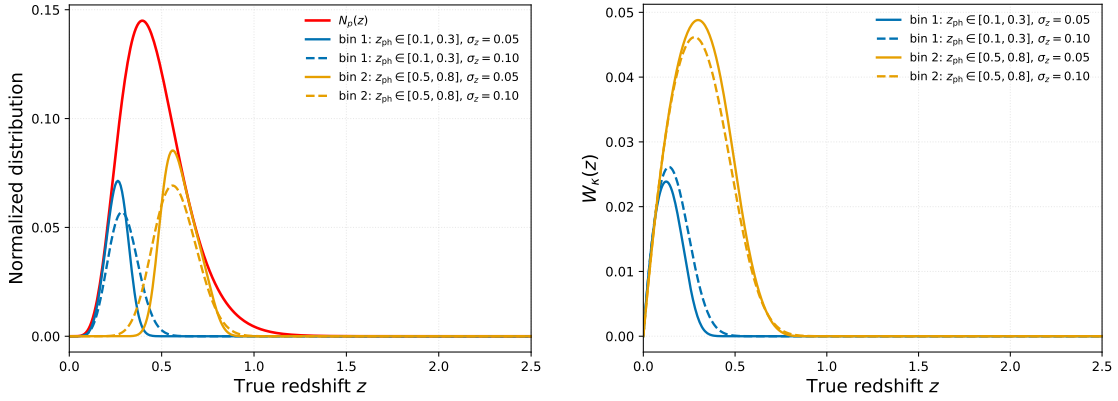


Figure 2: Left: it shows the distribution of the source. The dashed line represents the pessimistic case; Right: Kernel of weak lensing field

GR / Λ CDM

For the standard GR/ Λ CDM case, the growth equation reads

$$\frac{d^2 D}{da^2} + \left[\frac{3}{a} + \frac{1}{E(a)} \frac{dE(a)}{da} \right] \frac{dD}{da} - \frac{3}{2} \frac{\Omega_{m,0}}{a^5 E(a)^2} D = 0, \quad (3.4)$$

so that

$$\mathcal{D}_{\Lambda\text{CDM}}(a) = \frac{3}{a} + \frac{1}{E(a)} \frac{dE(a)}{da}, \quad \mathcal{S}_{\Lambda\text{CDM}}(a) = \frac{3}{2} \frac{\Omega_{m0}}{a^5 E(a)^2}. \quad (3.5)$$

Interacting dark energy (IDE)

For the IDE model with interaction term $Q = \Gamma(a) \rho_m$, the evolution of the matter contrast is

$$\frac{d^2 \delta_m}{da^2} + \left[\frac{3}{a} + \frac{1}{E(a)} \frac{dE(a)}{da} + \frac{\Gamma(a)}{aH_0 E(a)} \right] \frac{d\delta_m}{da} + \left[\frac{1}{a^2 H_0 E(a)} \frac{d(a\Gamma(a))}{da} + \frac{\Gamma(a)}{a^2 H_0 E(a)} - \frac{3}{2} \frac{\Omega_{m0}}{a^5 \beta(a) E(a)^2} \right] \delta_m = 0. \quad (3.6)$$

Identifying $D \equiv \delta_m$ and rearranging it into the form of equation 3.1, we obtain

$$\mathcal{D}_{\text{IDE}}(a) = \frac{3}{a} + \frac{1}{E(a)} \frac{dE(a)}{da} + \frac{\Gamma(a)}{aH_0 E(a)}, \quad (3.7)$$

$$\mathcal{S}_{\text{IDE}}(a) = \frac{3}{2} \frac{\Omega_{m0}}{a^5 \beta(a) E(a)^2} - \frac{1}{a^2 H_0 E(a)} \frac{d(a\Gamma(a))}{da} - \frac{\Gamma(a)}{a^2 H_0 E(a)}. \quad (3.8)$$

In the limit $Q \rightarrow 0$ ($\Gamma \rightarrow 0$), the extra terms vanish and $\mathcal{D}_{\text{IDE}} \rightarrow \mathcal{D}_{\Lambda\text{CDM}}$, $\mathcal{S}_{\text{IDE}} \rightarrow \mathcal{S}_{\Lambda\text{CDM}}$.

Hu–Sawicki $f(R)$

For Hu–Sawicki $f(R)$ gravity in the quasi-static, sub-horizon limit, the modified Poisson equation can be written as

$$-\frac{k^2}{a^2} \Phi(k, a) = 4\pi G \mu(a, k) \bar{\rho}_m(a) \delta_m(k, a), \quad (3.9)$$

where Φ is the Newtonian potential and $\mu(a, k)$ encodes the effective modification to the gravitational coupling. In GR/ Λ CDM one has $\mu(a, k) = 1$, while in Hu–Sawicki $f(R)$ the function $\mu(a, k)$ becomes scale dependent, enhancing gravity on scales below the Compton wavelength of the scalar degree of freedom and recovering $\mu \rightarrow 1$ on large scales. Incorporating effective factor $\mu(a, k)$, leading to

$$\frac{d^2 D}{da^2} + \left[\frac{3}{a} + \frac{1}{E(a)} \frac{dE(a)}{da} \right] \frac{dD}{da} - \frac{3}{2} \frac{\Omega_{m0}}{a^5 E(a)^2} \mu(a, k) D = 0. \quad (3.10)$$

Thus

$$\mathcal{D}_{f(R)}(a, k) = \frac{3}{a} + \frac{1}{E(a)} \frac{dE(a)}{da}, \quad \mathcal{S}_{f(R)}(a, k) = \frac{3}{2} \frac{\Omega_{m0}}{a^5 E(a)^2} \mu(a, k). \quad (3.11)$$

Equations (3.1)–(3.2) therefore offer a compact, physically transparent framework in which the drag term \mathcal{D}_X and the source term \mathcal{S}_X can be compared directly between Λ CDM, IDE, and Hu–Sawicki $f(R)$. Here $\mu(a, k)$

$$\mu(a, k) = 1 + \frac{1}{3} \frac{k^2}{k^2 + a^2 m^2(a)}, \quad (3.12)$$

with $m(a)$ the scalar-field mass (Compton wavenumber). For the Hu–Sawicki model with $n = 1$, the scalar-field mass is determined by the background through

$$m^2(a) = \frac{1}{2} H_0^2 \frac{[\Omega_{m0} a^{-3} + 4(1 - \Omega_{m0})]^3}{|f_{R0}| (\Omega_{m0} + 4(1 - \Omega_{m0}))^2}, \quad (3.13)$$

The above unified growth equations are solved by imposing initial conditions deep in the matter-dominated epoch, at a scale factor $a_i = 10^{-3}$, where all models considered reduce effectively to Einstein–de Sitter. In this regime, the growing-mode solution for the linear growth factor follows.

$$D(a) \propto a, \quad (3.14)$$

so that we adopt

$$D(a_i) = a_i, \quad \left. \frac{dD}{da} \right|_{a=a_i} = 1, \quad (3.15)$$

as common initial conditions for all scenarios. For GR/ Λ CDM and IDE the linear growth factor is scale independent, $D(a; k) \equiv D(a)$, whereas in Hu–Sawicki $f(R)$ gravity the modified Poisson equation induces a scale dependence, and we write $D(a; k)$ to emphasize this.

The logarithmic growth rate is then defined in general as

$$f(a; k) = \frac{d \ln D(a; k)}{d \ln a} = \frac{a}{D(a; k)} \frac{dD(a; k)}{da}. \quad (3.16)$$

In GR/ Λ CDM and IDE we simply have $f(a; k) \equiv f(a)$, while in Hu–Sawicki $f(R)$ the scale dependence of $D(a; k)$ leads to a corresponding scale dependence of the growth rate $f(a; k)$. This provides a convenient, dimensionless measure of the departure of structure growth from the Einstein–de Sitter behaviour and will be used below when comparing the different beyond- Λ CDM models.

Figure 1 illustrates explicitly how these unified growth equations translate into distinct time- and scale-dependent behaviour for the three scenarios considered. The left panel shows the redshift evolution of the growth-rate amplitude $f\sigma_8(z)$, defined in terms of the linear growth factor as

$$f\sigma_8(a) = a \frac{1}{\delta_m(1)} \frac{d\delta_m(a)}{da} \sigma_{8,0} \quad (3.17)$$

for GR/ Λ CDM, IDE, and Hu–Sawicki $f(R)$, all evolved from the common EdS initial conditions at ($a_i = 10^{-3}$). The curves coincide deep in the matter era and start to diverge once dark energy or modified gravity becomes dynamically important: the IDE model exhibits a modified late-time growth due to the interaction term $\Gamma(a)$, while Hu–Sawicki $f(R)$ tracks Λ CDM at the background level but already shows a slight excess in $f\sigma_8(z)$ in the linear regime because of the effective enhancement $\mu(a, k) > 1$ on the relevant scales.

In Fig. 1, left panel, we summarize the same information in terms of the growth-rate amplitude $f\sigma_8(z)$, which is more directly connected to large-scale structure observables such as redshift-space distortions and weak lensing. For each model we compute the logarithmic growth rate $f(a; k)$ from the unified equation and combine it with the corresponding linear root mean square (rms) fluctuation $\sigma_8(z)$ to obtain $f\sigma_8(z)$ as a function of redshift. The Λ CDM curve provides the reference, while IDE and Hu–Sawicki $f(R)$ deviate in characteristic ways: IDE modifies the redshift evolution primarily through changes in the drag and source terms at the background level, whereas Hu–Sawicki $f(R)$ produces an enhanced $f\sigma_8(z)$ due to the scale-dependent effective coupling $\mu(a, k)$. These differences in $f\sigma_8(z)$ propagate directly into the matter power spectrum and, through the lensing kernel, into the tomographic shear power spectra discussed in section 4.1.

The right panel of Fig. 1 focuses on the genuinely scale-dependent behaviour in Hu–Sawicki $f(R)$ by plotting $f(a; k)$ at fixed low redshift (here $z = 0.1$) as a function of

wavenumber k . On large scales ($k \ll a m(a)$), the modification function $\mu(a, k) \rightarrow 1$ and $D(a; k)$ approaches the GR/ Λ CDM result, while on smaller, quasi-linear scales ($k \gtrsim a m(a)$) the Yukawa-like enhancement of the effective gravitational strength drives an increase in the growth factor. This panel therefore makes explicit the role of $\mu(a, k)$ in turning the unified equation into a genuinely scale-dependent growth law in Hu–Sawicki $f(R)$, in contrast to the scale-independent $f(a)$ predicted by Λ CDM and IDE. We note the use of *FREmu* [47] to compute the $f(R)$ power spectrum. *FREmu* is rapid and precise emulator of power spectra specifically for the Hu–Sawicki $f(R)$ gravity model across scales $0.0089 h/\text{Mpc} < k < 0.5 h/\text{Mpc}$ and redshift range $0 < z < 3$ [47].

4 Weak lensing observables and observational systematics

In this section we summarize the weak lensing observables used in our analysis and discuss the principal systematic effects that affect current and forthcoming surveys.

4.1 Two-point power spectra

We describe the two-point statistics, namely the three-dimensional matter power spectrum and its projection into the weak lensing shear power spectrum measured by current and future galaxy surveys such as DES [13] and LSST [14]. Throughout, we work in a spatially flat universe and adopt the Limber and flat-sky approximations for projected fields.

The late-time clustering of matter is characterized by the three-dimensional matter power spectrum $P_\delta(k, z)$, defined via [48]

$$\langle \delta(\mathbf{k}, z) \delta^*(\mathbf{k}', z) \rangle = (2\pi)^3 \delta_{\mathbb{D}}(\mathbf{k} - \mathbf{k}') P_\delta(k, z), \quad (4.1)$$

where $\delta(\mathbf{x}, z)$ is the matter density contrast, $\delta_{\mathbb{D}}$ is the Dirac delta distribution, and $k = |\mathbf{k}|$ denotes the comoving wavenumber. In linear theory, the redshift dependence factorizes into an overall growth factor,

$$P_\delta^{\text{lin}}(k, z) = \left[\frac{D(a; k)}{D(a_{\text{ini}}; k)} \right]^2 P_\delta^{\text{lin}}(k, z_{\text{ini}}), \quad (4.2)$$

with $a = 1/(1+z)$ the scale factor, $D(a; k)$ the linear growth factor introduced in section. 3, and z_{ini} an early reference redshift in the matter-dominated era. For GR/ Λ CDM and IDE the growth is scale independent, so $D(a; k) \equiv D(a)$, whereas in Hu–Sawicki $f(R)$ gravity the modification of the Poisson equation induces a characteristic scale dependence $D(a; k)$.

On the quasi-linear and nonlinear scales probed by DES and LSST, we use the nonlinear matter power spectrum $P_\delta^{\text{NL}}(k, z)$ obtained from a combination of Boltzmann solvers (for the linear transfer) and nonlinear prescriptions (e.g. halo-model-based fitting formulae or emulators). In what follows we denote the model-dependent nonlinear matter spectrum by:

$$P_{\delta, X}^{\text{NL}}(k, z), \quad \text{where } X \in \{\Lambda\text{CDM}, w\text{CDM}, \text{IDE}, f(R)\}. \quad (4.3)$$

4.2 Tomographic weak lensing power spectrum

Weak gravitational lensing by large-scale structure induces coherent distortions in the observed shapes of background galaxies. For a source population with redshift distribution $n(z)$, the lensing convergence $\kappa(\boldsymbol{\theta})$ is given by a weighted line-of-sight projection of the matter density contrast [16, 49, 50],

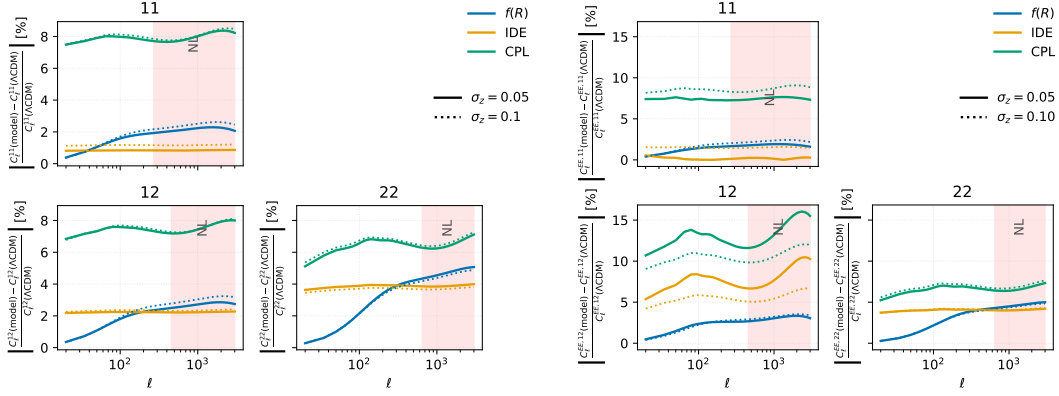


Figure 3: Left: percentage of deviation of $C_\ell^{\gamma\gamma}$ from the two tomographic bins using various models to Λ CDM Right: same but for $C_\ell^{\epsilon\epsilon}$

$$\kappa(\boldsymbol{\theta}) = \int_0^\infty dz \frac{c}{H(z)} W_\kappa(z) \delta(\chi(z)\boldsymbol{\theta}, z), \quad (4.4)$$

where $H(z)$ is the Hubble expansion rate and $\chi(z)$ is the comoving distance defined by

$$\chi(z) = \int_0^z \frac{c}{H(z')} dz'.$$

For a tomographic analysis, the source sample is divided into redshift bins labelled by $i = 1, \dots, N_{\text{tom}}$, each with normalized redshift distribution $n_i(z)$ satisfying

$$\int_0^\infty dz n_i(z) = 1.$$

The corresponding lensing kernel for bin i becomes

$$W_i(z) = \frac{3}{2} \frac{\Omega_{m,0} H_0^2}{c^2} \frac{\chi(z)}{a(z)} \int_z^\infty dz' p_i(z') \frac{\chi(z') - \chi(z)}{\chi(z')} \frac{c}{H(z')}, \quad (4.5)$$

Under the Limber and flat-sky approximations, the tomographic weak lensing (convergence or E-mode shear) angular power spectrum between bins i and j is given by [24, 51]

$$C_\ell^{ij} = \frac{c}{H_0} \int dz \frac{W_i(z) W_j(z)}{E(z) \chi^2(z)} P_\delta^{\text{NL}} \left(k = \frac{\ell + 1/2}{\chi(z)}, z \right), \quad (4.6)$$

where $C_\ell^{ij} \equiv C_\ell^{\kappa_i \kappa_j}$, and P_δ^{NL} is evaluated for the corresponding cosmological model X . In the absence of systematic effects and baryonic corrections, the E-mode shear power spectrum is equal to the convergence power spectrum, so we use the notation C_ℓ^{ij} interchangeably for $C_\ell^{\gamma_E^i \gamma_E^j}$ and $C_\ell^{\kappa_i \kappa_j}$.

In the subsequent sections, we combine these tomographic shear power spectra with higher-order statistics from the weak lensing bispectrum to constrain the beyond- Λ CDM models introduced above.

4.3 Intrinsic alignments (IA)

In this section, we present the modeling of the Intrinsic alignments (IA) whose full review can be found in [28]. IA arises from tidal gravitational interactions during galaxy formation, which induce correlated intrinsic orientations of galaxy shapes and contaminate weak-lensing measurements. Consequently, the observed ellipticity power spectrum contains several contributions beyond the true cosmic shear signal. An extensive description can be found in [24, 51]. The total two-point statistic can be decomposed as

$$C_{ij}^{\epsilon\epsilon}(\ell) = C_{ij}^{\gamma\gamma}(\ell) + C_{ij}^{I\gamma}(\ell) + C_{ij}^{\gamma I}(\ell) + C_{ij}^{II}(\ell), \quad (4.7)$$

where the additional terms correspond to correlations between intrinsic galaxy shapes and gravitational shear. These IA contributions are modeled through redshift integrals similar to the cosmic shear expression [28], for example

$$C_{ij}^{I\gamma}(\ell) = \frac{c}{H_0} \int dz \frac{W_i^{\text{IA}}(z) W_j^\gamma(z)}{E(z) \chi^2(z)} P_{\delta I} \left(\frac{\ell + 1/2}{\chi(z)}, z \right), \quad (4.8)$$

while the intrinsic alignment power spectra are related to the matter power spectrum through the following expressions [24, 51],

$$P_{\delta I}(k, z) = -\mathcal{A}_{\text{IA}} \rho_c \Omega_{m0} \frac{\mathcal{F}_{\text{IA}}(z)}{D(z)} P_{\delta\delta}(k, z), \quad (4.9)$$

$$P_{II}(k, z) = \left[-\mathcal{A}_{\text{IA}} \rho_c \Omega_{m0} \frac{\mathcal{F}_{\text{IA}}(z)}{D(z)} \right]^2 P_{\delta\delta}(k, z), \quad (4.10)$$

We choose $\mathcal{F}_{\text{IA}}(z) \sim 1$ following [24], while for the fiducial value of \mathcal{A}_{IA} we use $\mathcal{A}_{\text{IA}} = 5 \times 10^{-14} h^{-2} M_\odot \text{Mpc}^3$. Application to the case of bispectrum can also be found in [52].

4.4 Photometric redshift uncertainties

We adopt a survey configuration consistent with the expected properties of the Vera C. Rubin Observatory Legacy Survey of Space and Time (LSST). We use the Rubin observatory gold sample [14] such that the source galaxy redshift distribution is modeled as follows,

$$n(z) = \frac{1}{z_0} \left(\frac{z}{z_0} \right)^2 \exp[-(z/z_0)] \quad (4.11)$$

where $z_0 = 0.28$ for the 10-year survey parameters for the LSST gold sample. The lensing power spectra are constructed from galaxies divided into two tomographic redshift bins, $0 \leq z_1 \leq 1.3$ and $z_2 \geq 1.3$. For the survey specifications, we assume a sky coverage of $f_{\text{sky}} = 0.4$, consistent with the LSST wide-area survey ($\sim 18,000 \text{ deg}^2$), a mean galaxy number density $\bar{n}_g \simeq 26 \text{ arcmin}^{-2}$, and an rms intrinsic ellipticity per component of $\sigma_\epsilon = 0.26$. These values reflect realistic LSST Year-10 expectations.

We adopt a survey configuration consistent with the expected properties of the Vera C. Rubin Observatory Legacy Survey of Space and Time (LSST). We use the LSST gold sample [14] such that the source galaxy redshift distribution is modeled as follows:

$$n(z) = \frac{1}{z_0} \left(\frac{z}{z_0} \right)^2 \exp[-(z/z_0)] \quad (4.12)$$

where $z_0 = 0.28$ for the 10-year survey parameters for the LSST gold sample.

The lensing power spectra are constructed from galaxies divided into two tomographic redshift bins.

$$0 \leq z_1 \leq 1.3 \text{ and } z_2 \geq 1.3.$$

For the survey specifications, we assume a sky coverage of $f_{\text{sky}} = 0.4$, consistent with the LSST wide-area survey ($\sim 18,000 \text{ deg}^2$), a mean galaxy number density $\bar{n}_g \simeq 26 \text{ arcmin}^{-2}$, and an rms intrinsic ellipticity per component of $\sigma_\epsilon = 0.26$. These values reflect realistic LSST Year-10 expectations.

In photometric surveys such as LSST, the theoretical prediction of the tomographic shear signal depends on the true redshift distribution of source galaxies in each photometric bin, $n_i(z)$, since the lensing efficiency kernel is an integral over this distribution [19]. Photometric-redshift (photo- z) errors therefore represent a major systematic effect, as they distort the lensing kernel, induce leakage between tomographic bins, and bias the predicted shear power spectra C_ℓ^{ij} , potentially mimicking variations in cosmological parameters including the dark-energy equation-of-state parameter w if left unmodeled [53–55]. A particularly important source of bias arises from errors in the mean redshift of each bin, often parameterized as $n_i(z) \rightarrow n_i(z - \Delta z_i)$, while catastrophic outliers can introduce non-Gaussian tails in the redshift probability distribution $p(z|z_{\text{ph}})$ [18]. In this study we will use a fiducial photo- z error $\sigma_z = 0.05$ as a fiducial and $\sigma_z = 0.1$ for the pessimistic case.

5 Weak lensing bispectrum formalism

Beyond two-point statistics, the weak lensing bispectrum probes non-Gaussian features generated by nonlinear structure formation and modified growth, and therefore carries information that is largely complementary to the power spectrum.

5.1 Matter bispectrum modeling

The nonlinear clustering in the matter density fluctuations induces the matter bispectrum [56]. To model the matter bispectrum, we follow [57] and use the best available fitting formula for the matter bispectrum which is developed by [58] and is an extension of the formula in [56]. In this formula, the matter bispectrum is given by [56]

$$B^\delta(\mathbf{k}_{1,2,3}, z) = 2F_2(\mathbf{k}_1, \mathbf{k}_2, z)P_\delta(k_1, z)P_\delta(k_2, z) + 2\text{perms.}, \quad (5.1)$$

where $P_m(k, z)$ is the nonlinear matter power spectrum and, with $\mathbf{k}_1 \cdot \mathbf{k}_2 = k_1 k_2 \cos \theta$, the effective F_2 kernel is defined as

$$F_2(\mathbf{k}_i, \mathbf{k}_j, z) = \frac{5}{7}a(k_i)a(k_j) + \frac{1}{2} \frac{\mathbf{k}_i \cdot \mathbf{k}_j}{k_i k_j} \left(\frac{k_i}{k_j} + \frac{k_j}{k_i} \right) b(k_i)b(k_j) \\ + \frac{2}{7} \frac{(k_i \cdot k_j)^2}{k_i^2 k_j^2} c(k_i)c(k_j). \quad (5.2)$$

a, b, c are function of n_e as well. Their fitting function for these parameters in F_2 is given by,

$$a(n_e, k) = \frac{1 + \sigma_8^{a_6}(z)\sqrt{0.7Q_3(n_e)}(qa_1)^{n_e+a_2}}{1 + (qa_1)^{n_e+a_2}} \quad (5.3)$$

$$b(n_e, k) = \frac{1 + 0.2a_3(n_e + 3)(qa_7)^{n_e+3+a_8}}{1 + (qa_7)^{n_e+3.5+a_8}} \quad (5.4)$$

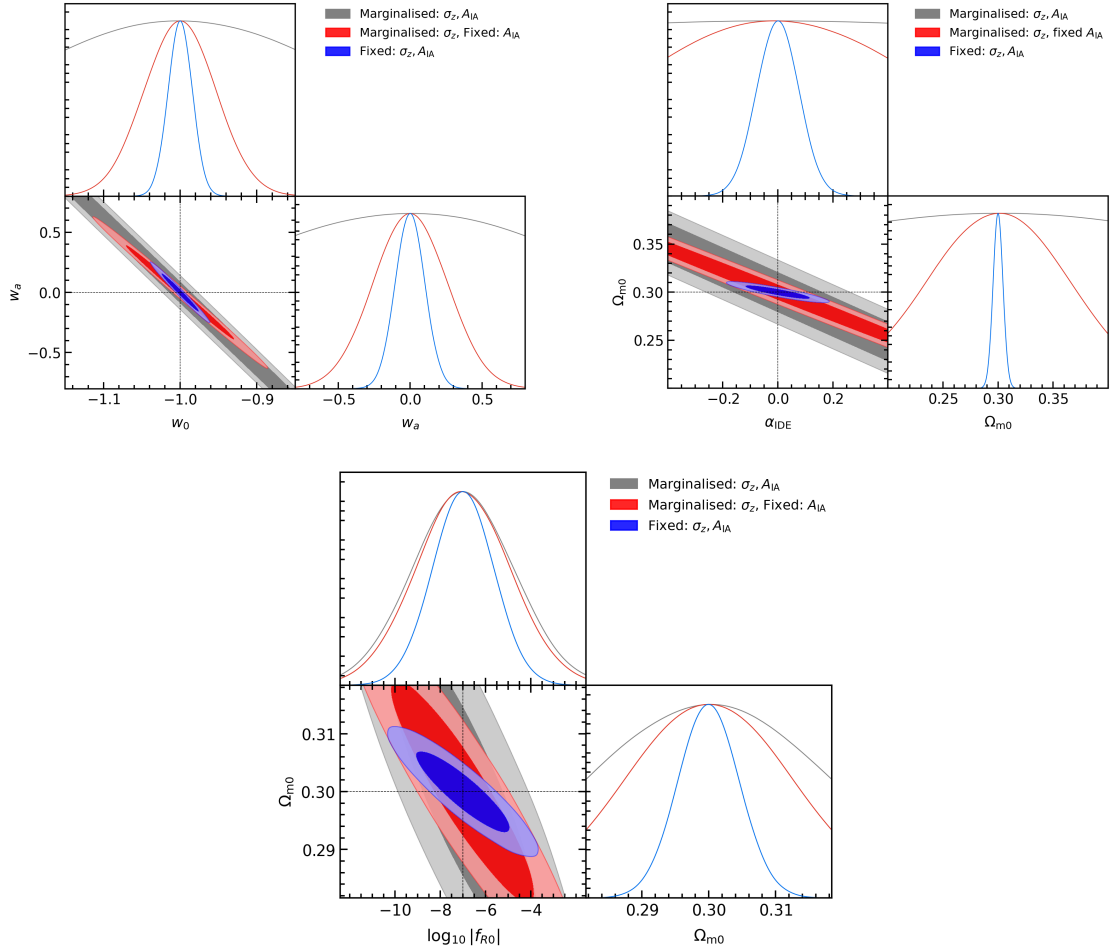


Figure 4: Ellipses for CPL, IDE and $f(R)$ from Power Spectrum

$$c(n_e, k) = \frac{1 + \left(\frac{4.5a_4}{1.5 + (n_e + 3)^4} \right) (qa_5)^{n_e + 3 + a_9}}{1 + (qa_5)^{n_e + 3.5 + a_9}} \quad (5.5)$$

where $n_e = d \ln P_m(k) / d \ln k$ is the effective spectral index of the power spectrum at the scale k , $q = k/k_{nl}$, $k_{nl} = \sqrt[3]{\frac{2\pi^3}{D(z)^2 P(k)}} = 0.2(1+z)^{2/(2+n_s)}$ and $Q_3(n_e) = (4 - 2^x)/(1 + 2^{x+1})$. The coefficients of the fitting formula a_i ($i = 1, 2, \dots, 9$) are obtained by fitting to the simulations in [58], and their best fit parameters are $a_1 = 0.484$, $a_2 = 3.740$, $a_3 = -0.849$, $a_4 = 0.392$, $a_5 = 1.013$, $a_6 = -0.575$, $a_7 = 0.128$, $a_8 = -0.722$, and $a_9 = -0.926$.

The total observed bispectrum (including intrinsic alignment contributions) is

$$B_{ijk}^{\text{obs}}(\ell_{123}) = B_{ijk}^{\gamma\gamma\gamma} + B_{ijk}^{\gamma\gamma I} + B_{ijk}^{\gamma II} + B_{ijk}^{III}. \quad (5.6)$$

5.2 Tomographic shear bispectrum

In addition to the shear power spectrum in the section 4.2, the three-point correlations of the lensing fields—captured by the shear bispectrum—provide complementary information on the nonlinear growth of structure and the non-Gaussian features of the matter distribution.

Considering the flat-sky approximation and Limber's equation, the bispectrum of the galaxy weak lensing shear field is defined as:

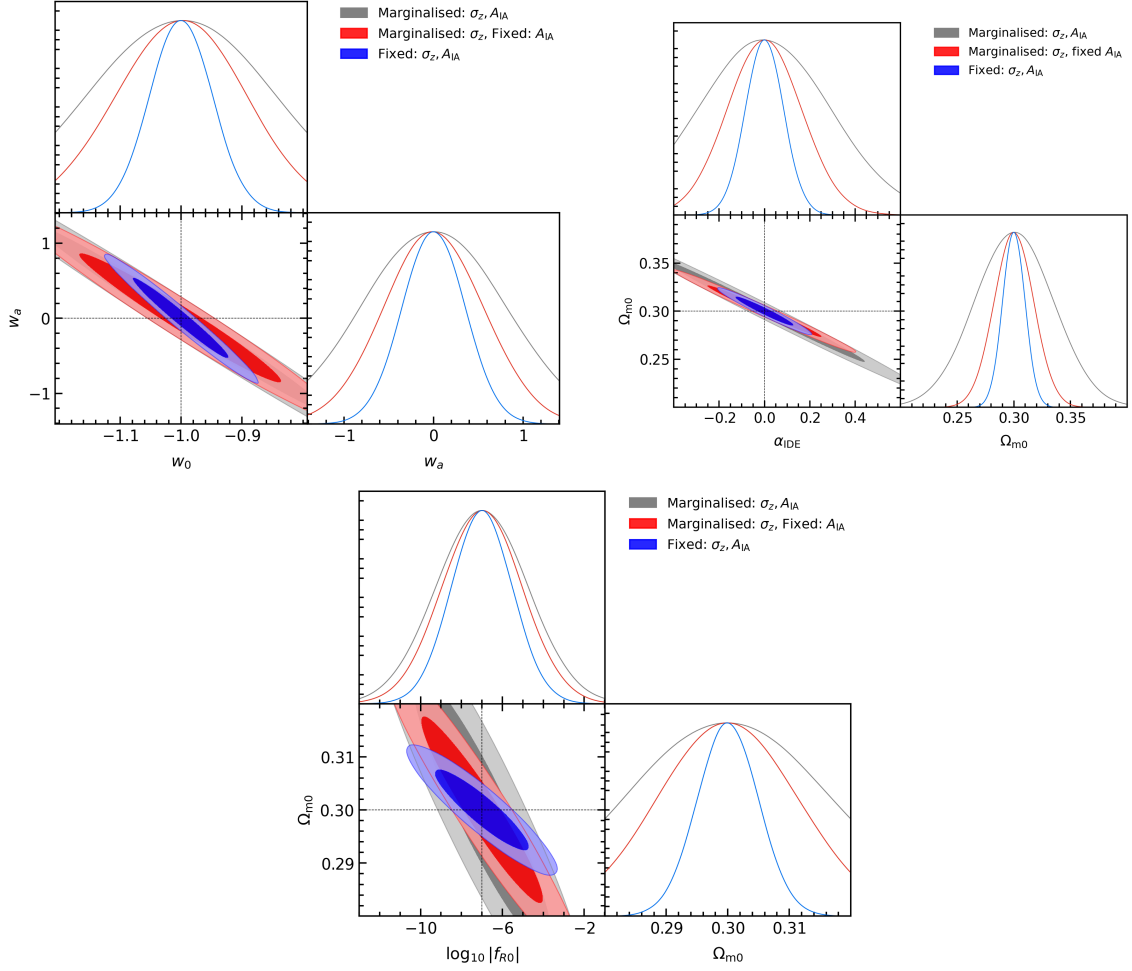


Figure 5: Ellipses for CPL, IDE and $f(R)$ from Bispectrum

$$\langle \gamma_{\ell_1} \gamma_{\ell_2} \gamma_{\ell_3} \rangle = (2\pi)^2 \delta_D(\ell_1 + \ell_2 + \ell_3) B^\gamma(\ell_1, \ell_2, \ell_3) \quad (5.7)$$

where $\langle \dots \rangle$ denotes the ensemble average. The multipoles satisfy the triangle condition, $|\ell_i - \ell_j| \leq \ell_k \leq \ell_i + \ell_j$. δ_D is the Dirac delta function. γ_ℓ is the Fourier mode of the shear lensing fields. The shear field is approximately calculated in the same way as the convergence lensing field. The lensing-mass field is the line-of-sight integral over the gravitational potential of the LSS, and is directly related to the matter inhomogeneities. The flat-sky lensing bispectrum is expressed in terms of the three-dimensional matter bispectrum (B^δ) as [59]

$$B_\gamma^{ijk}(\ell_{1,2,3}) = \int_0^{\chi_h} d\chi \frac{W_\gamma^i(\chi) W_\gamma^j(\chi) W_\gamma^k(\chi)}{\chi^4} B^\delta(\mathbf{k}_{1,2,3}, z(\chi)) \quad (5.8)$$

where $\mathbf{k} = \ell/\chi$ and $W_\gamma^i(\chi)$ is given in equation 4.5.

6 Fisher matrix formalism for power spectrum and bispectrum

We quantify parameter constraints using the Fisher information matrix, combining contributions from the tomographic power spectra and bispectra. For a data vector \mathbf{d} with covariance matrix \mathbf{C} and model parameters $\{\theta_\alpha\}$, the Fisher matrix is given by [60, 61]

$$F_{\alpha\beta} = \frac{1}{2} \text{Tr} \left[\mathbf{C}^{-1} \frac{\partial \mathbf{C}}{\partial \theta_\alpha} \mathbf{C}^{-1} \frac{\partial \mathbf{C}}{\partial \theta_\beta} \right] + \frac{\partial \boldsymbol{\mu}^T}{\partial \theta_\alpha} \mathbf{C}^{-1} \frac{\partial \boldsymbol{\mu}}{\partial \theta_\beta}, \quad (6.1)$$

where $\boldsymbol{\mu}$ denotes the theoretical mean (here, the vector of C_ℓ^{ij} and/or $B_{\ell_1 \ell_2 \ell_3}^{ijk}$). In the Gaussian approximation for the observables, and neglecting parameter dependence of the covariance, this reduces to a sum over multipoles and tomographic combinations.

6.1 Power spectrum Fisher matrix

The information is provided by the angular power spectra, which include contributions from cosmic shear (gravitational lensing), intrinsic alignments, and cross-correlations. The Fisher matrix is computed by summing over all multipoles ℓ in the observed range $[\ell_{\min}, \ell_{\max}]$ and over all possible combinations of field types A, B, C, D and tomographic redshift bins i, j, m, n . For a given multipole ℓ , the sensitivity to cosmological parameters θ_α and θ_β is computed from the derivatives of the angular power spectra $C_{ij}^{AB}(\ell)$ with respect to the cosmological parameters. The derivatives are weighted by the inverse of the full covariance matrix $\text{Cov}[C_{ij}^{AB}(\ell), C_{mn}^{CD}(\ell)]$, which includes the effect of cosmic variance, galaxy shape noise, and correlations between different observables and tomographic redshift bins. The Fisher matrix element $F_{\alpha\beta}$ represents the total information contained in the tomographic angular power spectrum data vector [24],

$$F_{\alpha\beta}^{ijmn} = \sum_{ABCD} \frac{\partial C_{ij}^{AB}(\ell)}{\partial \theta_\alpha} \text{Cov}^{-1}[C_{ij}^{AB}(\ell), C_{mn}^{CD}(\ell)] \frac{\partial C_{mn}^{CD}(\ell)}{\partial \theta_\beta}, \quad (6.2)$$

$$F_{\alpha\beta} = \sum_{ijmn} \sum_{\ell=\ell_{\min}}^{\ell_{\max}} F_{\alpha\beta}^{ijmn}. \quad (6.3)$$

Where f_{sky} is the fraction of sky surveyed, $\Delta\ell$ is the multipole bin width, and $C_\ell^{ij}(\ell)$ is the observed signal based on equation 4.6. In our case, where we have one tracer, the covariance matrix is as follows,

$$\text{Cov}[C_\ell^{ij}(\ell), C_\ell^{kl}(\ell')] = \frac{C_\ell^{ik}(\ell) C_\ell^{jl}(\ell') + C_\ell^{il}(\ell) C_\ell^{jk}(\ell')}{(2\ell + 1) f_{\text{sky}} \Delta\ell} \delta_{\ell\ell'}. \quad (6.4)$$

6.2 Bispectrum Fisher matrix

In this study, we consider only the Gaussian contribution to the covariance. The formulation of the covariance matrix, of the lensing bispectrum in [59], can be approximated as of the lensing bispectrum, can be written as follows,

$$\text{Cov}[B_{(ijk)}(\ell_{123}), B_{(i'j'k')}(\ell'_{1,2,3})] \approx \text{Cov}_G^{\text{BS}} \quad (6.5)$$

where that Gaussian contribution is the product of power spectra:

$$\begin{aligned} \text{Cov}_G^{\text{BS}} &= \frac{\Omega_s}{N_t(\ell_{123})} P_{ii'}^{\text{obs}}(\ell_1) P_{jj'}^{\text{obs}}(\ell_2) P_{kk'}^{\text{obs}}(\ell_3) \delta_{\ell_1 \ell_1}^K \delta_{\ell_2 \ell_2}^K \delta_{\ell_3 \ell_3}^K \\ &+ \{2 \text{ terms from permutations of } (i \leftrightarrow j, \ell_1 \leftrightarrow \ell_2)\} \\ &+ \{2 \text{ terms from permutations of } (i \leftrightarrow k, \ell_1 \leftrightarrow \ell_3)\}. \end{aligned} \quad (6.6)$$

$\Omega_s = 4\pi f_{\text{sky}}$ and the number of triangles is given as follows:

$$N_t(\ell_{123}) = \frac{\Omega_s^2 \ell_1 \ell_2 \ell_3 \Delta \ell_1 \Delta \ell_2 \Delta \ell_3}{2\pi^3 \sqrt{2\ell_1^2 \ell_2^2 + 2\ell_1^2 \ell_3^2 + 2\ell_2^2 \ell_3^2 - \ell_1^4 - \ell_2^4 - \ell_3^4}} \quad (6.7)$$

Following [57, 59], when considering lensing tomography with n_s redshift bins, we must account for different spectra for each multiple-bin or n -point configuration in order to include the full information content of the spectra. For the power spectrum, there are $n_s(n_s + 1)/2$ independent spectra for $i = j$, and $n_s(n_s - 1)/2$ cross-spectra for $i \neq j$.

The bispectrum case is more involved. For a general triangle configuration with $\ell_1 \neq \ell_2 \neq \ell_3$, we need to include n_s^3 bispectra corresponding to each triangle configuration (ℓ_1, ℓ_2, ℓ_3) . For two redshift bins ($n_s = 2$), we have

$$B_{(111)}, B_{(112)}, B_{(122)}, B_{(222)},$$

as well as all permutations such as $B_{(121)}$ and $B_{(212)}$. For isosceles triangles ($\ell_1 = \ell_2 \neq \ell_3$), the symmetry under permutations of (ℓ_1, ℓ_2) reduces the number of distinct configurations. For equilateral triangles ($\ell_1 = \ell_2 = \ell_3$), which we consider only in this study, additional symmetry further reduces the number of independent bispectra.

7 Analysis and discussion

This section focuses on the analysis of the departure from the Λ CDM model and on how the systematics affect the non- Λ CDM model, including their information content.

7.1 deviation from Λ CDM

Intrinsic alignment effects.

The right panel of figure 3 includes intrinsic alignment (IA) contributions. The observed shear power spectrum can be written as

$$C_\ell^{ij,\text{obs}} = C_\ell^{ij,\gamma\gamma} + C_\ell^{ij,\gamma I} + C_\ell^{ij,II}, \quad (7.1)$$

where $\gamma\gamma$ denotes the gravitational lensing term, while γI and II represent the intrinsic-gravitational and intrinsic-intrinsic contributions, respectively.

Intrinsic alignments primarily contaminate intermediate and small angular scales and become increasingly relevant at low redshift, where galaxy shapes are more strongly correlated with the local tidal field. Since IA traces the underlying matter density field, its amplitude depends on the growth function $D(a)$.

For $f(R)$ gravity, the enhanced growth at late times increases both the lensing signal and the IA contamination. However, because the gravitational enhancement is scale dependent, the relative fractional deviation with respect to Λ CDM remains more pronounced at high

multipoles. IA partially reduces the contrast by adding a contribution that scales similarly with the matter power spectrum, thereby absorbing part of the modified-gravity enhancement.

In IDE models, where deviations originate from modified growth rather than a modified Poisson equation, IA affects the signal in a more uniform manner across scales. Since both the shear and IA terms respond to the same altered growth history, the fractional deviation can either increase or decrease depending on the sign of the interaction parameter, but remains comparatively smooth in ℓ .

For the CPL model, IA introduces the largest relative modification of the fractional deviation at low redshift. Because CPL deviations are already small at high redshift and scale independent, the addition of IA—whose amplitude is strongest at low z —can artificially enhance or suppress the apparent deviation in the lowest tomographic bins. At higher redshift bins, where both dark energy effects and IA contributions diminish, the fractional deviation asymptotically approaches the Λ CDM prediction.

Photometric redshift uncertainties.

The effect of photometric redshift (photo- z) errors is illustrated by comparing the solid ($\sigma_z = 0.05$) and dotted ($\sigma_z = 0.10$) curves in Fig. 3. Increasing σ_z broadens the tomographic selection functions,

$$n_i(z) \rightarrow \tilde{n}_i(z) = \int dz' n_i(z') p(z|z'), \quad (7.2)$$

thereby smoothing the lensing kernel in equation 4.5.

This broadening reduces radial resolution, mixes adjacent bins, and partially suppresses scale-dependent features in the projected power spectra.

For the $f(R)$ model, where deviations arise from a scale-dependent modification of the effective gravitational coupling $\mu(a, k)$, the enhanced clustering at intermediate and high multipoles is partially diluted when σ_z increases. The smearing of the redshift distribution averages over epochs with different Compton scales, reducing the contrast with respect to Λ CDM. Consequently, the fractional deviation decreases slightly for larger photo- z uncertainties, particularly at high ℓ .

In the IDE scenario, where deviations stem from a modified growth history due to energy-momentum exchange in the dark sector, the effect is similar but weaker. Since the growth modification is primarily time dependent and only mildly scale dependent, photo- z broadening mainly reduces the tomographic contrast rather than altering the overall scale behavior.

For the CPL parametrization, the impact of photo- z uncertainties is minimal. Because CPL modifies only the background expansion and leaves the Poisson equation unchanged ($\mu = 1$), the growth remains scale independent. The photo- z smoothing therefore acts almost as a uniform amplitude suppression with little modification of the ℓ -dependence.

Overall, increasing σ_z systematically reduces the discriminating power between models by washing out tomographic information and suppressing the scale-dependent signatures that are most pronounced in modified-gravity scenarios.

The apparent scale dependence in IDE and CPL cross-bin spectra is not fundamental from the model. It arises because angular multipoles mix different physical scales and redshifts through line-of-sight projection, and because the growth deviation evolves with redshift. Cross-bin overlap enhances this effect.

In summary, photometric redshift uncertainties primarily degrade tomographic sensitivity and dilute scale-dependent signatures, while intrinsic alignments introduce an additional

growth-dependent contribution that can partially mask or mimic deviations from Λ CDM. The combined impact is most significant for modified-gravity models, where the signal relies on scale-dependent growth, and least significant for CPL-like background-only modifications.

7.2 Information content

The analysis of Figures 4 and 5 alongside Tables 1 and 2 reveals profound insights into cosmological constraints derived from weak lensing power spectrum and bispectrum analyses for various dark energy and modified gravity models. Figure 4 displays marginalized Fisher constraints obtained from the tomographic weak-lensing shear power spectrum for three beyond- Λ CDM scenarios: the Chevallier-Polarski-Linder (CPL) parametrization, Interacting Dark Energy (IDE) model, and Hu-Sawicki $f(R)$ gravity. The contours are presented in their respective two-parameter planes: (w_0, w_a) for CPL, (α, Ω_m) for IDE, and $(\ln |f_{R0}|, \Omega_m)$ for $f(R)$ models. Different colors and line styles represent various treatments of nuisance parameters, including marginalized versus fixed photometric redshift uncertainties (σ_z) and intrinsic alignment amplitudes (\mathcal{A}_{IA}). This figure highlights significant degeneracies between parameters for all models, with CPL showing a strong elongated contour in the (w_0, w_a) plane indicating degeneracy between the present-day equation-of-state parameter and its time evolution. For IDE, the (α, Ω_m) contours show a strong but slightly less severe degeneracy than CPL, while the $f(R)$ model exhibits the tightest and most distinctive constraints. Overall, Figure 4 demonstrates that power spectrum-only analysis is fundamentally limited by degeneracies between background expansion, growth amplitude, and nuisance systematics.

In contrast, Figure 5 presents marginalized Fisher constraints derived from weak lensing bispectrum analysis for the same three beyond- Λ CDM models, shown in identical two-parameter planes as Figure 4. Comparing Figure 5 with Figure 4 reveals that the bispectrum analysis generally offers more constrained results with smaller error ellipses and helps resolve parameter degeneracies. This indicates that higher-order statistics, like the bispectrum, provide complementary information that can improve cosmological constraints, especially for models where scale-dependent growth is significant. The bispectrum’s ability to probe non-Gaussian features generated by nonlinear structure formation provides information largely complementary to the power spectrum, helping to break degeneracies between parameters that are present in power spectrum-only analyses. The elongated contours in the (w_0, w_a) plane for CPL and (α, Ω_m) plane for IDE visible in Figure 4 are noticeably reduced in Figure 5, indicating a better separation of parameter values.

Table 1 provides quantitative Fisher constraints (standard deviations, σ) for key cosmological parameters of the $f(R)$, CPL, and IDE models based on power spectrum analysis, detailing how these constraints change under different treatments of nuisance parameters. For example, with fixed σ_z and \mathcal{A}_{IA} , $\sigma(\ln |f_{R0}|) = 1.357$, $\sigma(w_0) = 0.0159$, and $\sigma(\alpha) = 0.0764$. When σ_z and \mathcal{A}_{IA} are fully marginalized, these errors significantly increase, with $\sigma(\ln |f_{R0}|)$ becoming 2.236, $\sigma(w_0)$ becoming 0.2511, and $\sigma(\alpha)$ becoming 2.6895. This table quantifies the impact of nuisance parameters on parameter constraints, showing that marginalizing over intrinsic alignments and photometric redshift uncertainties significantly enlarges the error ellipses for all models, indicating that these systematics degrade the constraining power of the power spectrum. The $f(R)$ model is particularly sensitive to these nuisance parameters, as its constraints rely heavily on precise tomographic analysis and scale-dependent growth.

Table 2 presents quantitative Fisher constraints for the same cosmological parameters and models as Table 1, but derived from bispectrum analysis. With fixed σ_z and \mathcal{A}_{IA} , $\sigma(\ln |f_{R0}|) = 1.502$, $\sigma(w_0) = 0.0517$, and $\sigma(\alpha) = 0.08436$, and when σ_z and \mathcal{A}_{IA} are fully

marginalized, $\sigma(\ln |f_{R0}|)$ becomes 2.237, $\sigma(w_0)$ becomes 0.1557, and $\sigma(\alpha)$ becomes 0.2944. Comparing Table 2 with Table 1 reveals that bispectrum analysis generally yields tighter constraints for most parameters, even when nuisance parameters are marginalized. For instance, the marginalized $\sigma(w_0)$ for CPL is 0.1557 with bispectrum versus 0.2511 with power spectrum. This underscores the value of combining both two-point (power spectrum) and three-point (bispectrum) statistics to improve cosmological constraints and break parameter degeneracies, especially in the presence of systematic effects.

The model-specific constraint behavior reveals important distinctions. For the CPL model, both the power spectrum and bispectrum analyses show a pronounced elongation in the (w_0, w_a) plane, indicating a strong degeneracy between the present-day equation-of-state parameter and its time variation. The power spectrum primarily constrains a weighted combination of (w_0, w_a) due to similar effective expansion histories, leaving w_a weakly determined. The impact of photo- z uncertainties on CPL is minimal, mainly causing a uniform amplitude suppression rather than altering angular dependence, as CPL modifies only background expansion and leaves the Poisson equation unchanged. The Interacting Dark Energy model shows (α, Ω_m) contours with a strong, though slightly less severe, degeneracy compared to the CPL model. The interaction parameter α alters the effective matter evolution and continuously modifies growth history across redshift, and the bispectrum helps to reduce this degeneracy. Since IDE's growth modification remains scale-independent, the degeneracy with Ω_m cannot be fully broken by the power spectrum alone.

The Hu-Sawicki $f(R)$ gravity model yields the tightest and most distinctive constraints due to its genuine scale-dependent linear growth factor. The $(\ln |f_{R0}|, \Omega_m)$ contours show degeneracies in Figure 4, but the bispectrum significantly tightens these constraints, as seen in Figure 5. The enhanced growth at late times in $f(R)$ increases both the lensing signal and intrinsic alignment contamination, but the scale-dependent nature of the gravitational enhancement means \mathcal{A}_{IA} partially absorbs the modified-gravity enhancement, enlarging Fisher contours. Increasing photometric redshift uncertainties broadens tomographic selection functions, smoothing the lensing kernel and reducing radial resolution. This degrades tomographic sensitivity and dilutes scale-dependent signatures, with the effect being most significant for $f(R)$ models where precise tomographic resolution is crucial. The tables show that marginalizing over σ_z significantly increases the uncertainties for all parameters compared to fixed values. For example, $\sigma(\ln |f_{R0}|)$ increases from 1.357 to 2.088 for power spectrum and from 1.502 to 1.965 for bispectrum when σ_z is marginalized.

Intrinsic alignments introduce a growth-dependent contribution that can partially mask or mimic deviations from Λ CDM. \mathcal{A}_{IA} primarily contaminates intermediate and small angular scales and becomes more relevant at low redshift. Marginalizing over \mathcal{A}_{IA} further enlarges the error ellipses for all models, highlighting its significant impact. For $f(R)$ gravity, \mathcal{A}_{IA} partially absorbs the modified-gravity enhancement, enlarging Fisher contours. These findings demonstrate that while weak lensing is sensitive to scale-dependent growth modifications, its constraining power is significantly degraded by intrinsic alignments and photometric redshift uncertainties. The inclusion of bispectrum analysis helps to mitigate these issues, providing more robust and tighter constraints on cosmological parameters, particularly for models beyond Λ CDM.

Power spectrum			
Models	$f(R)$: $(\ln f_{R0} , \Omega_{m0})$	CPL: (w_0, w_a)	IDE: (α, Ω_{m0})
Fixed: $\sigma_z, \mathcal{A}_{IA}$	$\sigma(\ln f_{R0}) = 1.357$ $\sigma(\Omega_{m0}) = 0.0046$	$\sigma(w_0) = 0.0159$ $\sigma(w_a) = 0.1033$	$\sigma(\alpha) = 0.0764$ $\sigma(\Omega_{m0}) = 0.0045$
Fixed: \mathcal{A}_{IA} , Marginalised: σ_z	$\sigma(\ln f_{R0}) = 2.088$ $\sigma(\Omega_{m0}) = 0.01271$	$\sigma(w_0) = 0.0466$ $\sigma(w_a) = 0.2576$	$\sigma(\alpha) = 0.5758$ $\sigma(\Omega_{m0}) = 0.0656$
Marginalized: $\sigma_z, \mathcal{A}_{IA}$	$\sigma(\ln f_{R0}) = 2.236$ $\sigma(\Omega_{m0}) = 0.0184$	$\sigma(w_0) = 0.2511$ $\sigma(w_a) = 1.5446$	$\sigma(\alpha) = 2.6895$ $\sigma(\Omega_{m0}) = 0.3446$

Table 1: Fisher constraints from the power spectrum analysis under different nuisance parameter treatments.

Bispectrum			
Models	$f(R)$: $(\ln f_{R0} , \Omega_{m0})$	CPL: (w_0, w_a)	IDE: (α, Ω_{m0})
Fixed: $\sigma_z, \mathcal{A}_{IA}$	$\sigma(\ln f_{R0}) = 1.502$ $\sigma(\Omega_{m0}) = 0.005$	$\sigma(w_0) = 0.0517$ $\sigma(w_a) = 0.352$	$\sigma(\alpha) = 0.08436$ $\sigma(\Omega_{m0}) = 0.0099$
Fixed: \mathcal{A}_{IA} , Marginalised: σ_z	$\sigma(\ln f_{R0}) = 1.965$ $\sigma(\Omega_{m0}) = 0.011$	$\sigma(w_0) = 0.108$ $\sigma(w_a) = 0.561$	$\sigma(\alpha) = 0.165$ $\sigma(\Omega_{m0}) = 0.01752$
Marginalized: $\sigma_z, \mathcal{A}_{IA}$	$\sigma(\ln f_{R0}) = 2.237$ $\sigma(\Omega_{m0}) = 0.017$	$\sigma(w_0) = 0.1557$ $\sigma(w_a) = 0.8109$	$\sigma(\alpha) = 0.2944$ $\sigma(\Omega_{m0}) = 0.035$

Table 2: Fisher constraints from the bispectrum analysis under different nuisance parameter treatments.

8 Conclusion

This work presents an analysis to estimate how robust weak lensing spectra are beyond the Λ CDM paradigm and how sensitive the parameters of these models are to systematics, which are intrinsic alignment of galaxies and photometric redshift uncertainty. In order to focus more on the effect of the systematics, we consider Gaussian covariances, and for simplicity and symmetry, we consider then an equilateral configuration of the bispectrum as a complement to the power spectrum estimator.

Our findings regarding these two statistics on beyond- Λ CDM models, including the CPL parametrization, Interacting Dark Energy (IDE), and Hu-Sawicki $f(R)$ gravity, demonstrate that power-spectrum-only analyses are strongly affected by observational systematics: with fixed photometric redshift and intrinsic alignment parameters, the 1σ uncertainties are $\sigma(\ln |f_{R0}|) = 1.357$, $\sigma(w_0) = 0.0159$, and $\sigma(\alpha) = 0.0764$, whereas marginalizing over these systematics significantly increases the uncertainties to $\sigma(\ln |f_{R0}|) = 2.236$, $\sigma(w_0) = 0.2511$, and $\sigma(\alpha) = 2.6895$. In contrast, the weak-lensing bispectrum provides more robust constraints and effectively mitigates parameter degeneracies. With marginalized nuisance parameters, the bispectrum achieves $\sigma(\ln |f_{R0}|) = 2.237$, $\sigma(w_0) = 0.1557$, and $\sigma(\alpha) = 0.2944$, substantially improving constraints on IDE parameters and reducing the elongated degeneracies observed in the (w_0, w_a) and (α, Ω_m) planes. The Hu-Sawicki $f(R)$ model exhibits the tightest constraints due to its scale-dependent growth, which is effectively captured by higher-order statistics. Overall, our findings highlight the crucial role of combining two- and three-point weak-lensing statistics for breaking parameter degeneracies, mitigating systematic effects, and enhancing the robustness of cosmological constraints in future large-scale structure surveys.

These highlights that while weak lensing is sensitive to scale-dependent growth modifi-

cations, its constraint power can be significantly degraded by intrinsic alignments and photometric redshift uncertainties. This underscores the importance of robust systematic control and the use of complementary higher-order statistics to improve cosmological constraints.

The results presented in this work have relied on certain simplifications that could be relaxed in a subsequent study for a more comprehensive analysis. Including the non-Gaussian part of the variance and extending to more bispectrum configurations while adding more parameters will all make a more robust test of our estimators and improve their joint analysis.

9 Data Availability Statement

This manuscript has no associated observational data. Analysis products and intermediate data sets generated in this study are available from the authors upon reasonable request.

10 Code Availability Statement

Most of the analysis for this study is publicly available on the author's GitHub repository after the publication in: https://github.com/cbvaswar/Beyond_LCDM_WL/. Additional ancillary analysis codes can be obtained from the authors upon reasonable request.

11 Funding

LFR and CBV acknowledge the National Research Foundation (NRF), South Africa for supporting their postdoctoral research through grant funding, and the National Institute for Theoretical and Computational Sciences (NIThe CS) for additional financial support.

References

- [1] S. Bose, *Beyond Λ CDM: Exploring Alternatives to the Standard Cosmological Paradigm*. 2018, [10.1007/978-3-319-96761-5](https://arxiv.org/abs/10.1007/978-3-319-96761-5).
- [2] A. Albrecht et al., *Report of the Dark Energy Task Force*, [astro-ph/0609591](https://arxiv.org/abs/astro-ph/0609591).
- [3] D. Huterer and D. L. Shafer, *Dark energy two decades after: observables, probes, consistency tests*, *Reports on Progress in Physics* **81** (2017) 016901.
- [4] P. Bull et al., *Beyond Λ CDM: Problems, solutions, and the road ahead*, *Phys. Dark Univ.* **12** (2016) 56 [[1512.05356](https://arxiv.org/abs/1512.05356)].
- [5] L. Guzzo et al., *A test of the nature of cosmic acceleration using galaxy redshift distortions*, *Nature* **451** (2008) 541 [[0802.1944](https://arxiv.org/abs/0802.1944)].
- [6] S. M. Carroll, W. H. Press and E. L. Turner, *The Cosmological constant*, *Ann. Rev. Astron. Astrophys.* **30** (1992) 499.
- [7] SUPERNOVA COSMOLOGY PROJECT collaboration, S. Perlmutter et al., *Measurements of Ω and Λ from 42 High Redshift Supernovae*, *Astrophys. J.* **517** (1999) 565 [[astro-ph/9812133](https://arxiv.org/abs/astro-ph/9812133)].
- [8] SUPERNOVA SEARCH TEAM collaboration, A. G. Riess et al., *Observational evidence from supernovae for an accelerating universe and a cosmological constant*, *Astron. J.* **116** (1998) 1009 [[astro-ph/9805201](https://arxiv.org/abs/astro-ph/9805201)].
- [9] M. Ishak et al., *Modified Gravity and Dark Energy models Beyond $w(z)$ CDM Testable by LSST*, [1905.09687](https://arxiv.org/abs/1905.09687).

- [10] B. Jain and J. Khoury, *Cosmological Tests of Gravity*, *Annals Phys.* **325** (2010) 1479 [[1004.3294](#)].
- [11] V. Acquaviva and E. Gawiser, *How to Falsify the GR+LambdaCDM Model with Galaxy Redshift Surveys*, *Phys. Rev. D* **82** (2010) 082001 [[1008.3392](#)].
- [12] R. R. Caldwell, R. Dave and P. J. Steinhardt, *Cosmological imprint of an energy component with general equation of state*, *Phys. Rev. Lett.* **80** (1998) 1582 [[astro-ph/9708069](#)].
- [13] DES collaboration, T. M. C. Abbott et al., *Dark Energy Survey Year 6 Results: Cosmological Constraints from Cosmic Shear*, [2602.10065](#).
- [14] LSST Science Collaboration, P. A. Abell, e. Allison and al., *LSST Science Book, Version 2.0*, *arXiv e-prints* (2009) [arXiv:0912.0201](#) [[0912.0201](#)].
- [15] L. D. E. S. Collaboration et al., *Large synoptic survey telescope: dark energy science collaboration*, *arXiv preprint arXiv:1211.0310* (2012) .
- [16] J. Prat and D. Bacon, *Weak Gravitational Lensing*, [2501.07938](#).
- [17] S. Yuan, C. Pan, X. Liu, Q. Wang and Z. Fan, *Cosmological studies from tomographic weak lensing peak abundances and impacts of photo-z errors*, [1908.11493](#).
- [18] G. Bernstein and D. Huterer, *Catastrophic photometric redshift errors: weak lensing survey requirements*, *Mon. Not. Roy. Astron. Soc.* **401** (2010) 1399 [[0902.2782](#)].
- [19] LSST DARK ENERGY SCIENCE collaboration, T. Zhang, H. Almoubayyed, R. Mandelbaum, M. M. Rau, N. Šarčević, C. D. Leonard et al., *Forecasting the impact of source galaxy photometric redshift uncertainties on the LSST 3×2 pt analysis*, *Mon. Not. Roy. Astron. Soc.* **545** (2025) [staf1829](#) [[2507.01374](#)].
- [20] Z.-M. Ma, W. Hu and D. Huterer, *Effect of photometric redshift uncertainties on weak lensing tomography*, *Astrophys. J.* **636** (2005) 21 [[astro-ph/0506614](#)].
- [21] C. M. Hirata and U. Seljak, *Intrinsic alignment-lensing interference as a contaminant of cosmic shear*, *Phys. Rev. D* **70** (2004) 063526 [[astro-ph/0406275](#)].
- [22] J. Yao, E. M. Pedersen, M. Ishak, P. Zhang, A. Agashe, H. Xu et al., *Separating the intrinsic alignment signal and the lensing signal using self-calibration in photo-z surveys with KiDS450 and KV450 Data*, *Mon. Not. Roy. Astron. Soc.* **495** (2020) 3900 [[1911.01582](#)].
- [23] E. M. Pedersen, J. Yao, M. Ishak and P. Zhang, *First detection of the GI-type of intrinsic alignments of galaxies using the self-calibration method in a photometric galaxy survey*, *Astrophys. J. Lett.* **899** (2020) L5 [[1911.01614](#)].
- [24] EUCLID collaboration, A. Blanchard et al., *Euclid preparation. VII. Forecast validation for Euclid cosmological probes*, *Astron. Astrophys.* **642** (2020) A191 [[1910.09273](#)].
- [25] B. Joachimi et al., *Galaxy alignments: An overview*, *Space Sci. Rev.* **193** (2015) 1 [[1504.05456](#)].
- [26] D. Kirk et al., *Galaxy alignments: Observations and impact on cosmology*, *Space Sci. Rev.* **193** (2015) 139 [[1504.05465](#)].
- [27] A. Kiessling et al., *Galaxy Alignments: Theory, Modelling & Simulations*, *Space Sci. Rev.* **193** (2015) 67 [[1504.05546](#)].
- [28] C. Lamman, E. Tsaprazi, J. Shi, N. N. Šarčević, S. Pyne, E. Legnani et al., *The IA Guide: A Breakdown of Intrinsic Alignment Formalisms*, [2309.08605](#).
- [29] T. Kacprzak, J. Fluri, A. Schneider, A. Refregier and J. Stadel, *CosmoGridV1: a simulated Λ CDM theory prediction for map-level cosmological inference*, *JCAP* **02** (2023) 050 [[2209.04662](#)].
- [30] M. Yoon et al., *KiDS-1000 cosmic shear reanalysis using MetaCalibration*, [2510.01122](#).

- [31] J. J. Condon and A. M. Matthews, Λ CDM Cosmology for Astronomers, *Publ. Astron. Soc. Pac.* **130** (2018) 073001 [[1804.10047](#)].
- [32] M. Cortês and A. R. Liddle, *On desi's dr2 exclusion of λ cdm*, *Monthly Notices of the Royal Astronomical Society: Letters* **544** (2025) L121.
- [33] M. Benetti, P. T. Z. Seidel, C. Pigozzo, I. P. R. Baranov, S. Carneiro and J. C. Fabris, *Dark sector interactions in light of weak lensing data*, *JCAP* **06** (2025) 046 [[2410.07057](#)].
- [34] H. Wei, *Revisiting the Cosmological Constraints on the Interacting Dark Energy Models*, *Phys. Lett. B* **691** (2010) 173 [[1004.0492](#)].
- [35] W. Hu and I. Sawicki, *Models of $f(R)$ Cosmic Acceleration that Evade Solar-System Tests*, *Phys. Rev. D* **76** (2007) 064004 [[0705.1158](#)].
- [36] J.-H. Yan, Y. Gong, Q. Xiong, X. Chen, Q. Guo, M. Li et al., *Forecasting the Constraint on the Hu-Sawicki $f(R)$ Modified Gravity in the CSST 3×2 pt Photometric Survey*, *Astrophys. J.* **997** (2026) 357 [[2511.16097](#)].
- [37] C. B. V. Dash, T. G. Sarkar and A. K. Sarkar, *Intensity mapping of post-reionization 21-cm signal and its cross-correlations as a probe of $f(R)$ gravity*, *J. Astrophys. Astron.* **44** (2023) 5 [[2012.07373](#)].
- [38] A. De Felice and S. Tsujikawa, *$f(R)$ theories*, *Living Rev. Rel.* **13** (2010) 3 [[1002.4928](#)].
- [39] EUCLID collaboration, S. Casas et al., *Euclid: Constraints on $f(R)$ cosmologies from the spectroscopic and photometric primary probes*, [2306.11053](#).
- [40] V. K. Oikonomou and I. Giannakoudi, *A panorama of viable $F(R)$ gravity dark energy models*, *Int. J. Mod. Phys. D* **31** (2022) 2250075 [[2205.08599](#)].
- [41] M. Barroso Varela and Á. de la Cruz-Dombriz, *Implications of $f(R)$ gravity on late-time cosmic structure growth through a complete description of density perturbations*, *Phys. Dark Univ.* **51** (2026) 102232 [[2510.19569](#)].
- [42] M. Feix, A. Nusser and E. Branchini, *Growth Rate of Cosmological Perturbations at $z \sim 0.1$ from a New Observational Test*, *Phys. Rev. Lett.* **115** (2015) 011301 [[1503.05945](#)].
- [43] E. V. Linder, *Cosmic growth history and expansion history*, *Phys. Rev. D* **72** (2005) 043529 [[astro-ph/0507263](#)].
- [44] L. Pogosian and A. Silvestri, *The pattern of growth in viable $f(R)$ cosmologies*, *Phys. Rev. D* **77** (2008) 023503 [[0709.0296](#)].
- [45] Y. Gong, *The growth factor parameterization and modified gravity*, *Phys. Rev. D* **78** (2008) 123010 [[0808.1316](#)].
- [46] D. Benisty, *Quantifying the s_8 tension with the redshift space distortion data set*, *Physics of the Dark Universe* **31** (2021) 100766.
- [47] J. Bai and J.-Q. Xia, *FREmu: Power Spectrum Emulator for $f(R)$ Gravity*, *Astrophys. J.* **971** (2024) 11 [[2405.05840](#)].
- [48] S. Dodelson and F. Schmidt, *Modern Cosmology*. Academic Press, 2024.
- [49] M. Bartelmann and P. Schneider, *Weak gravitational lensing*, *Phys. Rept.* **340** (2001) 291 [[astro-ph/9912508](#)].
- [50] A. Refregier, *Weak gravitational lensing by large scale structure*, *Ann. Rev. Astron. Astrophys.* **41** (2003) 645 [[astro-ph/0307212](#)].
- [51] EUCLID collaboration, A. C. Deshpande et al., *Euclid preparation - XXXVI. Modelling the weak lensing angular power spectrum*, *Astron. Astrophys.* **684** (2024) A138 [[2302.04507](#)].
- [52] T. Bakx, A. Eggemeier, T. Kurita, N. E. Chisari and Z. Vlah, *The Bispectrum of Intrinsic Alignments: Theory Modelling and Forecasts for Stage IV Galaxy Surveys*, [2504.10009](#).

- [53] Z. Ma, W. Hu and D. Huterer, *Effects of Photometric Redshift Uncertainties on Weak-Lensing Tomography*, *ApJ* **636** (2006) 21 [[astro-ph/0506614](#)].
- [54] A. Amara and A. Refregier, *Systematic Bias in Cosmic Shear: Beyond the Fisher Matrix*, *Mon. Not. Roy. Astron. Soc.* **391** (2008) 228 [[0710.5171](#)].
- [55] A. Amara and A. Refregier, *Optimal Surveys for Weak Lensing Tomography*, *Mon. Not. Roy. Astron. Soc.* **381** (2007) 1018 [[astro-ph/0610127](#)].
- [56] R. Scoccimarro, H. M. P. Couchman and J. A. Frieman, *The Bispectrum as a Signature of Gravitational Instability in Redshift-Space*, *Astrophys. J.* **517** (1999) 531 [[astro-ph/9808305](#)].
- [57] M. Takada and B. Jain, *Cosmological parameters from lensing power spectrum and bispectrum tomography*, *Mon. Not. Roy. Astron. Soc.* **348** (2004) 897 [[astro-ph/0310125](#)].
- [58] H. Gil-Marín, C. Wagner, F. Fragkoudi, R. Jimenez and L. Verde, *An improved fitting formula for the dark matter bispectrum*, *Journal of Cosmology and Astro-Particle Physics* **2012** (2012) 047 [[1111.4477](#)].
- [59] I. Kayo and M. Takada, *Cosmological parameters from weak lensing power spectrum and bispectrum tomography: including the non-Gaussian errors*, [1306.4684](#).
- [60] A. F. Heavens, M. Seikel, B. D. Nord, M. Aich, Y. Bouffanais, B. A. Bassett et al., *Generalized Fisher matrices*, *Mon. Not. Roy. Astron. Soc.* **445** (2014) 1687 [[1404.2854](#)].
- [61] A. Heavens, *Statistical techniques in cosmology*, *arXiv e-prints* (2009) [arXiv:0906.0664](#) [[0906.0664](#)].